

Reconstructing Real-Valued Quantum States

Zhixin Song,^{1,*} Hang Ren,² Melody Lee,³ Bryan Gard,⁴ Nicolas Renaud,^{5,6} and Spencer H. Bryngelson^{3,7,8}

¹*School of Physics, Georgia Institute of Technology, Atlanta, GA, USA*

²*Berkeley Center for Quantum Information and Computation, Berkeley, CA, USA*

³*School of Computational Science & Engineering,
Georgia Institute of Technology, Atlanta, GA, USA*

⁴*CIPHER, Georgia Tech Research Institute, Atlanta, GA, USA*

⁵*Netherlands eScience Center, Matrix Building III, Amsterdam, The Netherlands*

⁶*Quantum Application Lab, Science Park, Startup Village, Amsterdam, The Netherlands*

⁷*Daniel Guggenheim School of Aerospace Engineering,
Georgia Institute of Technology, Atlanta, GA, USA*

⁸*George W. Woodruff School of Mechanical Engineering,
Georgia Institute of Technology, Atlanta, GA, USA*

(Dated: May 13, 2025)

Quantum tomography is a crucial tool for characterizing quantum states and devices and estimating nonlinear properties of the systems. Performing full quantum state tomography (FQST) on an N_q qubit system requires an exponentially increasing overhead with $\mathcal{O}(3^{N_q})$ distinct Pauli measurement settings to resolve all complex phases and reconstruct the density matrix. However, many appealing applications of quantum computing, such as quantum linear system algorithms, require only real-valued amplitudes. Here we introduce a novel readout method for real-valued quantum states that reduces measurement settings required for state vector reconstruction to $\mathcal{O}(N_q)$, while the post-processing cost remains exponential. This approach offers a substantial speedup over conventional tomography. We experimentally validate our method up to 10 qubits on the latest available IBM quantum processor and demonstrate that it accurately extracts key properties such as entanglement and magic. Our method also outperforms the standard SWAP test for state overlap estimation. This calculation resembles a numerical integration in certain cases and can be applied to extract nonlinear properties, which are important in application fields.

Introduction.—Efficient linear system solvers play a vital role in modern scientific computing and engineering challenges, from accelerating the training of large-scale machine learning models [1] to sophisticated fluid dynamics simulations [2]. Quantum approaches to linear system solves have garnered attention due to their potential to outperform classical methods [3, 4]. In particular, state-of-the-art quantum linear system algorithms (QLSA) [5–8] promise super-polynomial speedups in the fault-tolerant regime, where resource-intensive quantum error correction protocols and data encoding schemes such as block-encoding are required. Despite these advances, the quantum readout problem [9] may still limit the performance of many claims of potential quantum advantage. When studying quantum many-body systems, desired state properties can be extracted efficiently, including magnetization, correlation functions, and entanglement entropy [10]. In many other scientific problems where QLSA is favorable, however, the desired properties are nonlinear and involve non-Hermitian observables, making it challenging to construct a measurement scheme even using the powerful classical shadow tomography [11]. The typical approach is to reconstruct

the state through tomographic methods or amplitude estimation [12, 13] and then apply post-processing to extract the relevant properties [14, 15].

Efficient quantum state reconstruction is a central task in quantum information science, enabling characterization of quantum states and modeling of quantum devices [16–18]. The standard FQST method [19] requires an exponential number of measurement settings to iterate over the Pauli basis $\{\sigma_x, \sigma_y, \sigma_z\}$ in each qubit. Moreover, the post-processing typically relies on resource-intensive maximum likelihood estimation (MLE) to ensure the reconstructed state $\tilde{\rho}$ is physical [20].

Approaches have been developed to address the challenges in FQST. Some methods reduce measurement costs by exploiting the low-rank structure of density matrices using compressed sensing [21] or by leveraging limited entanglement structures [22]. More recent techniques combine parallel measurements to further decrease required resources, as seen in quantum overlapping tomography [23, 24], with tensor network learning approaches [25–27]. However, these methods either rely on assumptions about the quan-

tum state's structure or involve additional learning processes with unclear post-processing scaling.

We show that for QLSA solves involving only real-valued states, reconstructing such states requires a linear number of measurement settings instead of an exponential overhead. Real-valued states arise naturally in many other quantum algorithms, including Grover's search [28] and the Bernstein–Vazirani algorithm [29]. With carefully injected resource states, one can achieve universal computation [30].

Similar ideas have been explored for real-valued observables in the context of classical shadow tomography [31]. This work introduces the *Hadamard Random Forest* (HRF) as a technique for reconstructing real-valued quantum states. By restricting the relative phase from a complex number to $\{\pm 1\}$, HRF resolves the phases exclusively in the σ_x basis combined with a specialized random forest algorithm [32]. We validate this approach on IBM's quantum hardware for up to 10 qubits and compare its performance against FQST for up to 5 qubits. In these experiments, HRF outperforms FQST in reconstruction accuracy and runtime. HRF also accurately estimates state properties, including quantum entanglement, magic, and state overlap from near-term hardware sampling results. These results fully support the practical hardware application of HRF.

Reconstructing quantum states.— Given an N_q qubit density matrix ρ , it can be expanded as,

$$\rho = \frac{1}{2^{N_q}} \sum_{i,j,\dots,\ell=0}^3 c_{ij\dots\ell} \underbrace{\sigma_i^{(1)} \otimes \sigma_j^{(2)} \dots \otimes \sigma_\ell^{(N_q)}}_{N_q \text{ qubit global observable}}, \quad (1)$$

where $c_{ij\dots\ell} \in \mathbb{C}$ and each $\sigma_0 = I, \sigma_{1,2,3} = \sigma_{x,y,z}$. After collecting 3^{N_q} global measurement statistics (each contains 2^{N_q} outcomes), the post-processing involves a maximum likelihood estimation (MLE) to ensure the reconstructed state $\tilde{\rho}$ is physical, i.e. positive semi-definite $\tilde{\rho} \geq 0$ with unit trace $\text{Tr}(\tilde{\rho}) = 1$ as illustrated in fig. 1.

Consider an N_q qubit real-valued state

$$|\psi\rangle = U_{\text{prep.}} |0\rangle^{\otimes N_q} = \sum_{j=0}^{2^{N_q}-1} \psi_j |j\rangle, \quad (2)$$

where $U_{\text{prep.}}$ is the unitary corresponding to the state preparation circuit and $\psi_j = \text{sgn}(\psi_j) \cdot |\psi_j| \in \mathbb{R}$. The basis states $|j\rangle$ are ordered according to the lexicographical order of their bit-string representations. HRF reconstructs the corresponding state vector by sampling $N_q + 1$ circuits. The first circuit measures

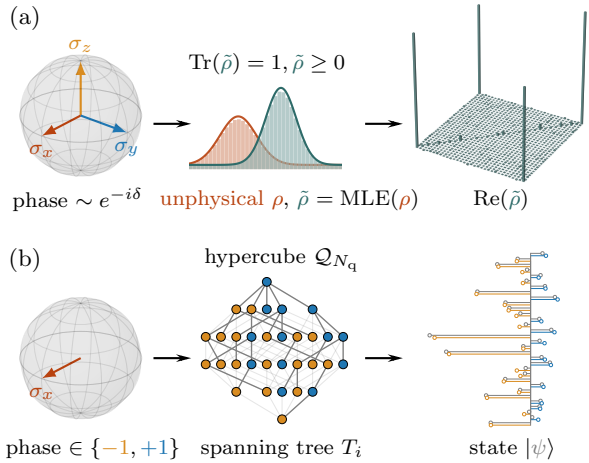


FIG. 1: Comparison between FQST (a) and the present HRF method (b) for an $N_q = 5$ case. FQST requires measuring each qubit in the Pauli basis, resulting in $3^5 = 243$ measurement settings. HRF only requires 6.

in the standard computational σ_z basis, evaluating the amplitudes $|\psi_j|$ by sampling the probability distribution $\{|\psi_j|^2\}$. Then, one measures each qubit in the σ_x basis, resulting in an additional N_q circuits to sample, which can be achieved by adding a Hadamard gate to rotate the measurement basis (see [33] for qubit ordering and circuit construction). Applying a Hadamard gate on the $(N_q - k - 1)$ -th qubit and sampling the output leads to the new amplitude vector $|\psi^k\rangle$, where ψ_j^k and $\psi_{j+2^k}^k$ contain the superposition of original amplitudes as

$$\psi_{j,j+2^k}^k = \frac{1}{\sqrt{2}} (\psi_j \pm \psi_{j+2^k}). \quad (3)$$

This computation leads to $(N_q + 1) \times (2^{N_q})$ total probabilities. One determines the relative signs between two amplitudes $s_{j,j+2^k} := \text{sgn}(\psi_j \psi_{j+2^k})$ by querying the sampling results $\{|\psi_j^k|^2\}_{k=0}^{N_q-1}$ as

$$s_{j,j+2^k} = \text{sgn} \left[\underbrace{2|\psi_j^k|^2}_{\text{new prob.}} - \underbrace{|\psi_j|^2 - |\psi_{j+2^k}|^2}_{\text{original prob.}} \right]. \quad (4)$$

All 2^{N_q} signs ($s_j := \text{sgn}(\psi_j)$) follow by tracing the path from the root amplitude ψ_0 (assuming $\psi_0 > 0$) to the nodes ψ_j and repeatedly applying the sign determination procedure of (4). Identifying such paths is equivalent to finding spanning trees T_i on the hypercube graph \mathcal{Q}_{N_q} with 2^{N_q} nodes and $N_q 2^{(N_q-1)}$ edges. The edge exists only when the node index differs by a power of 2. For example, \mathcal{Q}_5 contains 80 edges (light gray) as illustrated in fig. 2 (a).

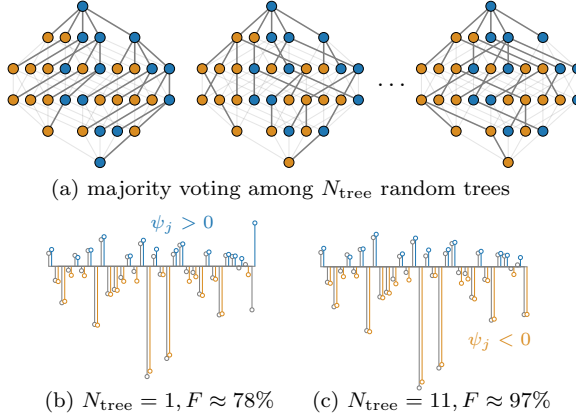


FIG. 2: Demonstration of using multiple spanning trees T_i to form a random forest and deploy a majority voting scheme to determine the signs. (a) Spanning trees in \mathcal{Q}_5 . The dark blue color is $\text{sgn}(\psi_j) = +1$ and light orange is $\text{sgn}(\psi_j) = -1$. (b) For a single tree, the last three signs are incorrectly determined. (c) No sign error for 11 trees.

\mathcal{Q}_{N_q} has at least $\Omega(2^{2^{N_q}-N_q-1})$ spanning trees [34]. The tree structure follows Pascal’s triangle using a breadth-first search (BFS) approach for computational efficiency. This structure ensures the tree depth is bounded from above by $L = N_q$. We collect the sign determination results of N_{tree} randomly generated spanning trees, then employ a majority voting scheme with a vote threshold of 50%. The full HRF algorithm is included in the End Matter [33]. The pre-processing step is independent of the quantum state structure, including rank and sparsity, and only depends on the system size N_q . The tree generation time has an exponential cost as the minimal operation on a graph is $\Omega(V)$, where V is the number of nodes. While generating the tree has an exponential cost, it is a one-time computation. Once constructed, the tree can be reused for any N_q qubit configuration.

Next, we analyze the error bounds of using different sample sizes $N_{\text{samp.}}$ and random trees N_{tree} . First, we estimate the probability of a single sign error between ψ_j and ψ_{j+2^k} is $\Pr(\tilde{s}_{j,j+2^k} \neq s_{j,j+2^k}) \leq \exp(-2N_{\text{samp.}}|\psi_j|^2|\psi_{j+2^k}|^2)$ according to the Hoeffding’s inequality, where \tilde{s} is the estimated sign using HRF. Figure 3 (a) shows that the larger the product $\psi_j\psi_{j+2^k}$, the easier it becomes to resolve their relative sign with fewer shots. Then, one can analyze the error propagation on each tree. Since every sign at node j is determined by a unique path of edges from the root ψ_0 of length $d_j \leq L$, the estimated \tilde{s}_j is the product of the estimated relative signs along this path. If any edge on the path has an

inference error, then the estimated sign flips parity for an odd number of errors. Assuming (for simplicity) that each edge has the same error probability $p_e := \Pr(\tilde{s}_{j,j+2^k} \neq s_{j,j+2^k})$ and errors are independent, the probability p_j that \tilde{s}_j is incorrect can be calculated as

$$p_j \leq \frac{1 - (1 - 2p_e)^L}{2}. \quad (5)$$

In the regime $p_e L \ll 1$, one recovers $p_j \approx p_e L$. But a moderate $p_e = 0.01$ can lead to unreliable predictions deeper in the tree at 10 qubits as $p_j \approx 0.1$. By combining N_{tree} random trees, the effective error rate becomes exponentially smaller. Assuming that each tree has an independent error rate $p_j < 1/2$, the probability of returning the wrong signs after majority voting is

$$\text{Pr}_{\text{HRF}}(\tilde{s}_j \neq s_j) \leq \exp(-2N_{\text{tree}}(1/2 - p_j)^2). \quad (6)$$

If each tree has error rate $p_j = 0.1$ independently, then $N_{\text{tree}} = 11$ trees suffice for a sign error below 3%, as shown in fig. 3 (b). If one allows the error budget to be a small fraction of the nodes δ have sign errors, we require $N_{\text{samp.}} \geq \ln(L/\delta)/(2m^2)$ to maintain $p_j < 1/2$ and $N_{\text{tree}} \geq \ln(1/\delta)/(2(1/2 - p_j)^2)$, where $m = \min_{j,k} \psi_j \psi_{j+2^k}$ is the minimal overlap.

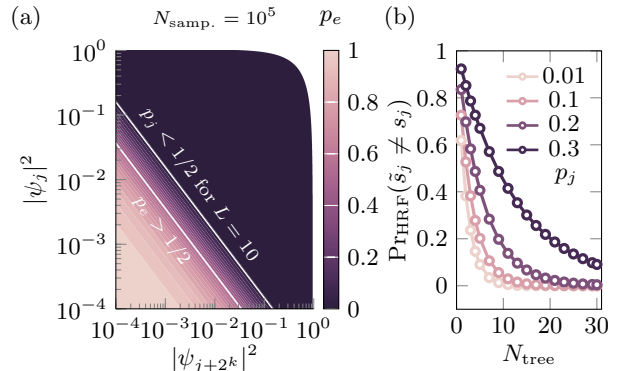


FIG. 3: (a) Probability p_e of returning a sign error between node j and $j + 2^k$ using 10^5 samples, where the variables are constrained with $|\psi_j|^2 + |\psi_{j+2^k}|^2 \leq 1$. For 10 qubit states ($L = 10$), it requires $p_e < 0.05$ such that $p_j < 1/2$ and each tree behaves better than a random guess. (b) Probability of estimating the sign s_j wrong after majority voting with different p_j and N_{tree} .

Experiments.— We demonstrate the HRF method and compare its performance and runtime scaling with that of standard FQST in the Pauli basis on `ibm_fez`, the latest IBM Heron r2 superconducting quantum processor. Figure 4 (e) shows the readout and native two-qubit gate (CZ) error rates. We select

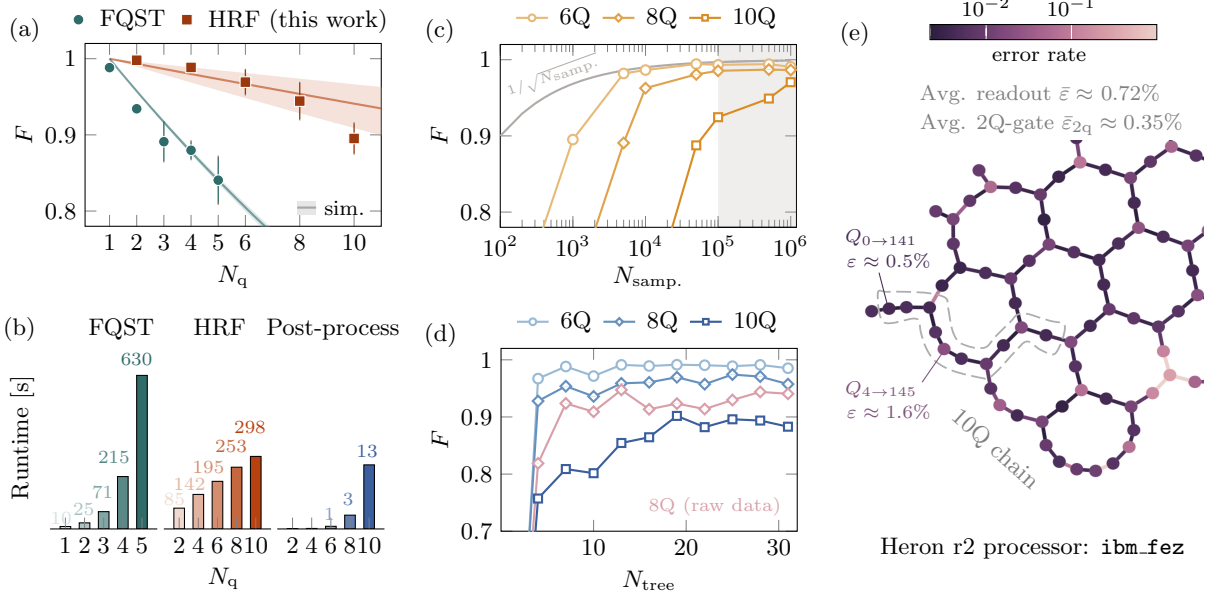


FIG. 4: (a) The fidelities of the reconstructed state with those obtained from FQST and HRF method running on `ibm_fez` quantum processor. (b) Runtime (seconds) scaling of FQST, HRF on `ibm_fez` and post-processing time using 111 trees. (c) The impact of samples N_{samp} to fidelities on noisy simulator. The gray line represents the upper bound limited by finite sampling noise $\epsilon \approx 1/\sqrt{N_{\text{samp}}}$, and $N_{\text{samp}} = 10^5$ is the maximal sample size used in experiments. (d) The impact of the number of trees N_{tree} used in post-processing for sign determination based on samples with and without error mitigation. (e) Readout error ϵ and 2 qubit gate error $\bar{\epsilon}_{2q}$, and single-qubit error $\epsilon_{1q} \sim 10^{-4}$.

a 10 qubit chain from the device to ensure a lower readout error, which is the dominant error source. The real-valued quantum states were generated using the hardware-efficient ansatz [35], but the gate set is limited to $R_y(\theta_j)$ rotation gates on each qubit and $\text{CNOT}_{j,j+1}$ on adjacent qubits. To minimize the influence of two-qubit gate errors, we use a constant shallow depth state preparation circuit U_{prep} , that consists of 4 layers of R_y gates and $4(N_q - 1)$ pairwise CNOT gates inside. We use measurement error mitigation for both the FQST and HRF experiments by inversion of an assignment matrix [36]. We adopt the X_+X_- dynamical decoupling sequence [37–39] to suppress decoherence during qubit idling time.

For FQST cases, we reconstruct the density matrix ρ up to 5 qubits by measuring 3^{N_q} global observables with $N_{\text{samp.}} = 10^4$ samples for each observable. The 5 qubit FQST experiment takes about 10 min to measure $3^5 = 243$ observables on `ibm_fez`. In contrast, HRF requires only 18 s of sampling time. The experiments were performed sequentially without interruption from periodic calibrations. Thus, the total running time, including error mitigation overhead, accurately reflects the circuit execution time, providing a faithful measure of the protocol’s efficiency and the experimental resources required.

Performing FQST for up to 10 qubits can be time-consuming (~ 6 h) on actual hardware. For HRF, we reconstruct the state vector $|\psi\rangle$ up to 10 qubits by sampling $N_q + 1 = 11$ circuits with $N_{\text{samp.}} = 10^5$ samples for $N_q > 5$ and $N_{\text{samp.}} = 10^4$ samples for $N_q \leq 5$ to ensure fair fidelity comparison with FQST. The transpiled 10 qubit circuit is $2.54\ \mu\text{s}$ long and the average T_2 coherence time on the 10 qubit chain of `ibm_fez` is $135.74\ \mu\text{s}$. We provide more detailed hardware calibration information in the End Matter [33]. Noisy simulations conducted in this study use the same calibration data.

Results.— We have three main experimental results. First, we confirm the feasibility of HRF in real-valued state reconstruction and demonstrate its superiority over FQST in terms of accuracy and runtime scaling. Figure 4 (a) shows the fidelity $F(\rho, \tilde{\rho}) = \text{Tr} [\sqrt{\sqrt{\rho}\tilde{\rho}\sqrt{\rho}}]^2$ between the exact state ρ and reconstructed state from hardware $\tilde{\rho}$, where $\tilde{\rho} = |\tilde{\psi}\rangle\langle\tilde{\psi}|$ for HRF. The average fidelity among $R = 5$ random states reaches 84.05% for 5 qubit FQST and 89.53% for 10 qubit HRF after 2.43×10^6 and 1.10×10^6 total samples, respectively. These experimental results are consistent with the noisy simulations shown in the shaded region using $R = 10$ random states. HRF exhibits a higher average fi-

dentity with fewer samples, but also exhibits higher variance due to randomness in post-processing. In other words, the reconstructed state has lower statistical bias with respect to the true fidelity of 1, but may exhibit higher variance due to fewer measurement shots. This bias–variance trade-off is common in quantum state tomography on noisy devices [24]. In practice, the community often prioritizes reducing bias over variance, as bias represents a systematic error, whereas variance can be suppressed by averaging over more samples [40].

Figure 4 (b) presents the linear runtime scaling for sample collection using $N_{\text{samp.}} = 10^5$ and a $\Omega(2^{N_q})$ scaling in post-processing, where the latter part can leverage parallel computing to distribute the workload on multiple CPUs since \mathcal{Q}_{N_q} is always bipartite [34]. The largest FQST reconstruction takes 3.35 h post-processing time for a 14-qubit state [41] while HRF would take only ~ 10 min post-processing time for the same problem size using $N_{\text{tree}} = 300$.

We show the impact of sample size $N_{\text{samp.}}$ and the number of trees N_{tree} in **fig. 4** (c) and (d) via simulations. The 10 qubit HRF fidelity could further reach 97.05% using $N_{\text{samp.}} = 10^6$ samples on a noisy simulator. As the state size increases, more samples are required to reach the finite sampling limit, as indicated by the gray curve. We observe that as more samples are collected, the estimated fidelity converges rapidly and asymptotically approaches the limit set by the sampling noise. This suggests that fluctuations in protocol performance are primarily due to statistical noise, with no additional sources of error, indicating the protocol’s efficiency and stability. For post-processing, the reconstructed state fidelity converges after doing majority voting using $N_{\text{tree}} \approx 30$ spanning trees on the corresponding hypercube graph. As illustrated in the pink curve (raw samples without error mitigation), higher-fidelity sampling data with measurement error mitigation would impact the final reconstructed state fidelity $\sim 3\%$. The overhead introduced is a few extra hardware calibrations, which require approximately 10 s for 10 qubit states.

Finally, we apply the HRF method to evaluate non-linear state properties including the logarithmic negativity $E_N(\rho)$ for entanglement quantification [42], α -stabilizer Rényi entropy $M_\alpha(|\psi\rangle)$ for quantifying quantum magic [43], and overlap $S_\ell(|\psi\rangle)$ between a classical index state $|\psi_\ell\rangle$ that resembles a numerical integration along the path ℓ . **Figure 5** (a) compares

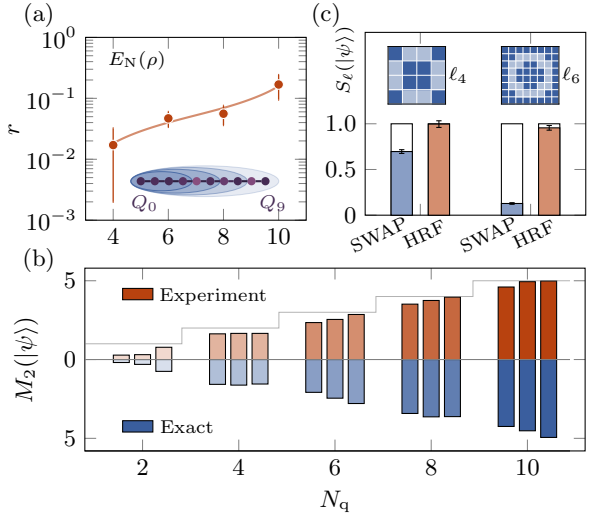


FIG. 5: Estimating quantum state properties using the reconstructed state $|\tilde{\psi}\rangle$ from HRF. (a) Log-negativity of $N_q \in \{4, 6, 8, 10\}$ on the 10-qubit chain of `ibm_fez`. (b) Stabilizer entropy of $R = 3$ random states on `ibm_fez`. (c) State overlap (noisy simulation) that resembles a numerical integration over a circle in the domain, where ℓ_4 and ℓ_6 are integration paths for 4- and 6-qubit.

the logarithmic negativity

$$E_N(\tilde{\rho}) = \log_2 \|\tilde{\rho}^{\Gamma_A}\|_1 \quad (7)$$

calculated from HRF (on `ibm_fez`) and exact values, where ρ^{Γ_A} is the partial transpose with respect to $[N_q/2]$ qubits subsystem A and $\|\cdot\|_1$ denotes the trace norm. The relative difference r is defined as $|E_N(\rho) - E_N(\tilde{\rho})|/|E_N(\rho)|$. The predicted value from the HRF method agrees well with the exact numerical value, except for the 10 qubit case. On the other side, magic states are the resource that allows quantum computers to attain an advantage over classical computers. One common magic measure is the α -stabilizer Rényi entropy [43], defined as

$$M_\alpha(|\psi\rangle) = \frac{1}{1-\alpha} \log_2 \left(\sum_{\sigma \in \mathcal{P}} 2^{-N_q} \langle \psi | \sigma | \psi \rangle^{2\alpha} \right), \quad (8)$$

where α is the entropic index and \mathcal{P} is the set of 4^{N_q} Pauli strings. Given its importance, we measure the 2-stabilizer entropy $M_2(|\tilde{\psi}\rangle)$ of 3 random real-valued states on `ibm_fez`, as shown in **fig. 5** (b). The results closely match an exact evaluation.

We also use HRF to estimate the overlap $S_\ell(|\psi\rangle) = |\langle \psi_{N_q} | \psi \rangle|^2$ where $\{\ell_{N_q}\}$ is a circle path in a 2D lattice of size $[2^{N_q/2}, 2^{N_q/2}]$ as illustrated in **fig. 5** (c),

and $|\psi_{\ell_{N_q}}\rangle = \frac{1}{N} \sum_{j \in \{\ell_{N_q}\}} |j\rangle$ is the corresponding state by concatenating the lattice row-wise for a normalization constant N . This quantity resembles a numerical integration over the path ℓ_{N_q} , which can occur, for example, when calculating drag and lift coefficients for computational fluid mechanics simulations [14], scattering cross sections in electromagnetism simulations [44], among others. We compare the estimated overlap with the standard SWAP test [45] through noisy simulations. The SWAP test requires $2N_q + 1$ qubits in total, and the explicit circuit construction with estimated hardware execution time is shown in fig. 7 [33]. The accuracy of the SWAP test decreases with increasing problem size N_q due to hardware noise, whereas HRF maintains a high fidelity of $\geq 95\%$ (averaged over 5 random states).

Conclusion.— We present an asymptotically faster technique for reconstructing real-valued quantum states. This method, HRF, reduces the exponential measurement settings in FQST from an exponential number to a linear one. Still, the post-processing time remains exponential, though it can be mitigated via parallel computing on classical devices. We experimentally demonstrate our approach on an IBM superconducting quantum processor. Using the superposition of amplitudes and a random forest algorithm as a post-processing tool, we reconstruct the random 10 qubit real-valued states with high fidelity $F \approx 89\%$. HRF accurately estimates state properties such as quantum entanglement, magic, and state overlap estimation from near-term hardware sampling results. This improvement paves the way for end-to-end applications based on QLSA and many application problems on near-term and early fault-tolerant devices. The method may also shed light on other techniques for strictly real-valued quantum tomography such as process tomography.

Data availability.— The code used for this manuscript is permissively (MIT) licensed and available at <https://github.com/comp-physics/Quantum-HRF-Tomography>.

Acknowledgments.— We acknowledge the use of IBM Quantum services for this work. The views expressed are those of the authors and do not reflect the official policy or position of IBM or the IBM Quantum team. This research used resources of the Oak Ridge Leadership Computing Facility, which is a DOE Office of Science User Facility supported under Contract DE-AC05-00OR22725.

* zsong300@gatech.edu

- [1] J. Liu, M. Liu, J.-P. Liu, Z. Ye, Y. Wang, Y. Alexeev, J. Eisert, L. Jiang, Towards provably efficient quantum algorithms for large-scale machine-learning models, *Nature Communications* **15** (2024) 434.
- [2] X. Li, X. Yin, N. Wiebe, J. Chun, G. K. Schenter, M. S. Cheung, J. Mülmenstädt, Potential quantum advantage for simulation of fluid dynamics, *Physical Review Research* **7** (2025) 013036.
- [3] M. R. Hestenes, E. Stiefel, Methods of conjugate gradients for solving linear systems, *Journal of Research of the National Bureau of Standards* **49** (1952).
- [4] Y. Saad, M. H. Schultz, Gmres: A generalized minimal residual algorithm for solving nonsymmetric linear systems, *SIAM Journal on Scientific and Statistical Computing* **7** (1986) 856–869.
- [5] A. M. Childs, R. Kothari, R. D. Somma, Quantum algorithm for systems of linear equations with exponentially improved dependence on precision, *SIAM Journal on Computing* **46** (2017) 1920–1950.
- [6] P. C. Costa, D. An, Y. R. Sanders, Y. Su, R. Babush, D. W. Berry, Optimal scaling quantum linear-systems solver via discrete adiabatic theorem, *PRX Quantum* **3** (2022) 040303.
- [7] G. H. Low, Y. Su, Quantum linear system algorithm with optimal queries to initial state preparation, *arXiv preprint arXiv:2410.18178* (2024).
- [8] M. E. Morales, L. Pira, P. Schleich, K. Koor, P. Costa, D. An, A. Aspuru-Guzik, L. Lin, P. Rebentrost, D. W. Berry, Quantum linear system solvers: A survey of algorithms and applications, *arXiv preprint arXiv:2411.02522* (2024).
- [9] S. Aaronson, Read the fine print, *Nature Physics* **11** (2015) 291–293.
- [10] H.-Y. Huang, R. Kueng, J. Preskill, Predicting many properties of a quantum system from very few measurements, *Nature Physics* **16** (2020) 1050–1057.
- [11] H.-Y. Huang, Learning quantum states from their classical shadows, *Nature Reviews Physics* **4** (2022) 81–81.
- [12] D. Grinko, J. Gacon, C. Zoufal, S. Woerner, Iterative quantum amplitude estimation, *npj Quantum Information* **7** (2021) 52.
- [13] A. Manzano, D. Musso, Á. Leitao, Real quantum amplitude estimation, *EPJ Quantum Technology* **10** (2023) 1–24.
- [14] J. Penuel, A. Kataharwa, P. D. Johnson, C. Farquhar, Y. Cao, M. C. Garrett, Feasibility of accelerating incompressible computational fluid dynamics simulations with fault-tolerant quantum computers, *arXiv preprint arXiv:2406.06323* (2024).
- [15] A. Patterson, L. Lapworth, Measurement schemes for quantum linear equation solvers, *Quantum Science and Technology* **10** (2025) 025037.
- [16] R. Blume-Kohout, T. Proctor, K. Young, Quantum characterization, verification, and validation, *arXiv preprint arXiv:2503.16383* (2025).
- [17] H. Ren, Y. Li, Modeling quantum devices and the reconstruction of physics in practical systems, *Physical*

- Review Letters **123** (2019) 140405.
- [18] R. Shaffer, H. Ren, E. Dyrenkova, C. G. Yale, D. S. Lobser, A. D. Burch, M. N. Chow, M. C. Revelle, S. M. Clark, H. Häffner, Sample-efficient verification of continuously-parameterized quantum gates for small quantum processors, *Quantum* **7** (2023) 997.
- [19] U. Leonhardt, Quantum-state tomography and discrete wigner function, *Physical Review Letters* **74** (1995) 4101.
- [20] Z. Hradil, Quantum-state estimation, *Physical Review A* **55** (1997) R1561.
- [21] D. Gross, Y.-K. Liu, S. T. Flammia, S. Becker, J. Eisert, Quantum state tomography via compressed sensing, *Physical Review Letters* **105** (2010) 150401.
- [22] M. Cramer, M. B. Plenio, S. T. Flammia, R. Somma, D. Gross, S. D. Bartlett, O. Landon-Cardinal, D. Poulin, Y.-K. Liu, Efficient quantum state tomography, *Nature Communications* **1** (2010) 149.
- [23] J. Cotler, F. Wilczek, Quantum overlapping tomography, *Physical Review Letters* **124** (2020) 100401.
- [24] Z. Yang, S. Ru, L. Cao, N. Zheludev, W. Gao, Experimental demonstration of quantum overlapping tomography, *Physical Review Letters* **130** (2023) 050804.
- [25] M. K. Kurmapu, V. Tiunova, E. Tiunov, M. Ringbauer, C. Maier, R. Blatt, T. Monz, A. K. Fedorov, A. Lvovsky, Reconstructing complex states of a 20-qubit quantum simulator, *PRX Quantum* **4** (2023) 040345.
- [26] Y. Guo, S. Yang, Quantum state tomography with locally purified density operators and local measurements, *Communications Physics* **7** (2024) 322.
- [27] C.-K. Hu, C. Wei, C. Liu, L. Che, Y. Zhou, G. Xie, H. Qin, G. Hu, H. Yuan, R. Zhou, et al., Experimental sample-efficient quantum state tomography via parallel measurements, *Physical Review Letters* **133** (2024) 160801.
- [28] L. K. Grover, A fast quantum mechanical algorithm for database search, in: Proceedings of the Twenty-Eighth Annual ACM Symposium on the Theory of Computing, 1996, pp. 212–219.
- [29] E. Bernstein, U. Vazirani, Quantum complexity theory, in: Proceedings of the twenty-fifth annual ACM symposium on Theory of computing, 1993, pp. 11–20.
- [30] N. Delfosse, P. Allard Guerin, J. Bian, R. Raussendorf, Wigner function negativity and contextuality in quantum computation on rebits, *Physical Review X* **5** (2015) 021003.
- [31] M. West, A. A. Mele, M. Larocca, M. Cerezo, Real classical shadows, arXiv preprint arXiv:2410.23481 (2024).
- [32] T. K. Ho, Random decision forests, in: Proceedings of 3rd international conference on document analysis and recognition, volume 1, IEEE, 1995, pp. 278–282.
- [33] See the supplemental material for more details. (2025).
- [34] F. Harary, J. P. Hayes, H.-J. Wu, A survey of the theory of hypercube graphs, *Computers & Mathematics with Applications* **15** (1988) 277–289.
- [35] A. Kandala, A. Mezzacapo, K. Temme, M. Takita, M. Brink, J. M. Chow, J. M. Gambetta, Hardware-efficient variational quantum eigensolver for small molecules and quantum magnets, *Nature* **549** (2017) 242–246.
- [36] P. D. Nation, H. Kang, N. Sundaresan, J. M. Gambetta, Scalable mitigation of measurement errors on quantum computers, *PRX Quantum* **2** (2021) 040326.
- [37] V. Tripathi, H. Chen, M. Khezri, K.-W. Yip, E. Levenson-Falk, D. A. Lidar, Suppression of crosstalk in superconducting qubits using dynamical decoupling, *Physical Review Applied* **18** (2022) 024068.
- [38] S. Niu, A. Todri-Sanial, Effects of dynamical decoupling and pulse-level optimizations on ibm quantum computers, *IEEE Transactions on Quantum Engineering* **3** (2022) 1–10.
- [39] N. Ezzell, B. Pokharel, L. Tewala, G. Quiroz, D. A. Lidar, Dynamical decoupling for superconducting qubits: A performance survey, *Physical Review Applied* **20** (2023) 064027.
- [40] C. Schwemmer, L. Knips, D. Richart, H. Weinfurter, T. Moroder, M. Kleinmann, O. Gühne, Systematic errors in current quantum state tomography tools, *Physical Review Letters* **114** (2015) 080403.
- [41] Z. Hou, H.-S. Zhong, Y. Tian, D. Dong, B. Qi, L. Li, Y. Wang, F. Nori, G.-Y. Xiang, C.-F. Li, et al., Full reconstruction of a 14-qubit state within four hours, *New Journal of Physics* **18** (2016) 083036.
- [42] M. B. Plenio, Logarithmic negativity: a full entanglement monotone that is not convex, *Physical Review Letters* **95** (2005) 090503.
- [43] L. Leone, S. F. Oliviero, A. Hamma, Stabilizer rényi entropy, *Physical Review Letters* **128** (2022) 050402.
- [44] B. D. Clader, B. C. Jacobs, C. R. Sprouse, Preconditioned quantum linear system algorithm, *Physical Review Letters* **110** (2013) 250504.
- [45] H. Buhrman, R. Cleve, J. Watrous, R. De Wolf, Quantum fingerprinting, *Physical Review Letters* **87** (2001) 167902.
- [46] V. Havlíček, A. D. Córcoles, K. Temme, A. W. Harrow, A. Kandala, J. M. Chow, J. M. Gambetta, Supervised learning with quantum-enhanced feature spaces, *Nature* **567** (2019) 209–212.
- [47] Y. Liu, S. Arunachalam, K. Temme, A rigorous and robust quantum speed-up in supervised machine learning, *Nature Physics* **17** (2021) 1013–1017.
- [48] A. Elben, B. Vermersch, R. Van Bijnen, C. Kokail, T. Brydges, C. Maier, M. K. Joshi, R. Blatt, C. F. Roos, P. Zoller, Cross-platform verification of intermediate scale quantum devices, *Physical Review Letters* **124** (2020) 010504.
- [49] F. Mintert, M. Kuś, A. Buchleitner, Concurrence of mixed multipartite quantum states, *Physical Review Letters* **95** (2005) 260502.
- [50] A. K. Ekert, C. M. Alves, D. K. Oi, M. Horodecki, P. Horodecki, L. C. Kwek, Direct estimations of linear and nonlinear functionals of a quantum state, *Physical Review Letters* **88** (2002) 217901.

End Matter

Generating the Random Forest

We include pseudocode in [algorithm 1](#) to describe the algorithm used in the main text.

Algorithm 1 Hadamard Random Forest (HRF)

Require: Number of qubits N_q , sample size for each circuit $N_{\text{samp.}}$, number of trees N_{tree}

Ensure: Reconstruct real state vector $|\psi\rangle \in \mathbb{R}^{2^{N_q}}$

▷ 1. Collect samples

- 1: Prepare $N_{\text{samp.}}$ copies of $|\psi\rangle$ using $U_{\text{prep.}}$.
- 2: Measure all N_q qubits in σ_z basis
- 3: **for all** $j \in \{0, \dots, 2^{N_q} - 1\}$ **do**
- 4: $|\tilde{\psi}_j|^2 \leftarrow$ empirical frequency in basis $|j\rangle$
- 5: **end for**
- 6: **for** $k = 0$ to $N_q - 1$ **do**
- 7: Prepare $N_{\text{samp.}}$ copies of $|\psi\rangle$ using $U_{\text{prep.}}$
- 8: Measure the $(N_q - k - 1)$ -th qubit in σ_x basis
- 9: Measure the rest qubits in σ_z basis
- 10: **for all** $j \in \{0, \dots, 2^{N_q} - 1\}$ **do**
- 11: $|\tilde{\psi}_j^k|^2 \leftarrow$ empirical frequency in basis $|j\rangle$
- 12: **end for**
- 13: **end for**

▷ 2. Build random forest

- 14: **for** $i = 1$ to N_{tree} **do**
- 15: $T_i \leftarrow$ a random spanning tree on \mathcal{Q}_{N_q} using BFS
- 16: Initialize root sign $s_0^{(i)} \leftarrow +1$
- 17: **for all** unique path from node 0 $\rightarrow j$ in T_i **do**
- 18: **for all** valid (n, k) along path **do**
- 19: Compute relative signs
- 20: $s_{n,n+2^k}^{(i)} \leftarrow \text{sgn}(2|\tilde{\psi}_n^k|^2 - |\tilde{\psi}_n|^2 - |\tilde{\psi}_{n+2^k}|^2)$
- 21: $s_j^{(i)} \leftarrow s_{j,j-2^k}^{(i)} \times \dots \times s_{2^k,0}^{(i)} \times s_0^{(i)}$
- 22: **end for**
- 23: **end for**
- 24: **end for**

▷ 3. Majority voting

- 25: **for all** $j \in \{0, \dots, 2^{N_q} - 1\}$ **do**
- 26: $s_j \leftarrow \text{sgn}\left(\sum_{i=1}^{N_{\text{tree}}} s_j^{(i)}\right)$
- 27: **end for**

▷ 4. Reconstruct state

- 28: **for all** $j \in \{0, \dots, 2^{N_q} - 1\}$ **do**
- 29: $|\tilde{\psi}_j| \leftarrow \sqrt{|\tilde{\psi}_j|^2}$
- 30: $\tilde{\psi}_j \leftarrow s_j \times |\tilde{\psi}_j|$
- 31: **end for**
- 32: **return** $|\tilde{\psi}\rangle$

Quantum Circuit for SPAM

We use the hardware efficient ansatz to prepare real-valued states as shown in [fig. 6](#). The parameters are chosen uniformly from interval $[-\pi/2, \pi/2]$.

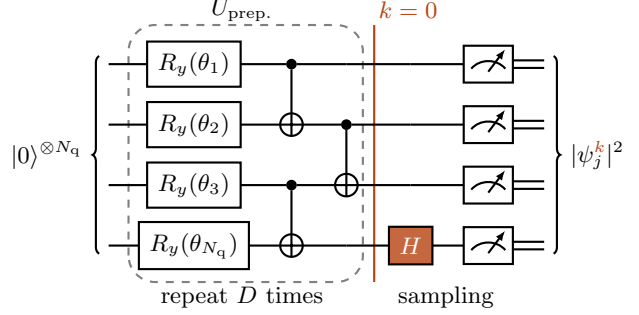


FIG. 6: State preparation and measurement (SPAM) circuits for HRF. The largest case contains 36 CZ gates.

Hardware Calibration Data

Here we provide the detailed hardware calibration data used in this study in [table I](#).

Qubit	T_1 (μs)	T_2 (μs)	Meas. error ε	2Q gate error ε_{2Q}
Q_0	184	101	4.64×10^{-3}	2.74×10^{-3}
Q_1	188	237	4.88×10^{-3}	2.69×10^{-3}
Q_2	216	173	4.39×10^{-3}	3.02×10^{-3}
Q_3	171	248	6.34×10^{-3}	3.35×10^{-3}
Q_4	142	111	1.56×10^{-2}	3.35×10^{-3}
Q_5	197	31	5.62×10^{-3}	3.48×10^{-3}
Q_6	170	152	9.28×10^{-3}	5.54×10^{-3}
Q_7	140	138	4.15×10^{-3}	3.42×10^{-3}
Q_8	154	111	1.29×10^{-2}	3.65×10^{-3}
Q_9	98	57	4.64×10^{-3}	/
Avg.	166	136	7.24×10^{-3}	3.47×10^{-3}

TABLE I: Device properties of `ibm_fez` at the time each experiment reported in this paper was performed. The readout length is $t_{\text{mea.}} = 1560$ ns and native 2Q gate (CZ) with pulse length $t_{2Q} = 84$ ns for all qubits.

Quantum Amplitude Estimation

Compared to quantum amplitude estimation (QAE) [12, 13], HRF employs shallow circuits with easily implementable gates. QAE is optimal for estimating a specific amplitude or few dominant amplitudes, but it requires deep, coherent circuits with controlled unitaries, which are challenging to implement and prone to errors. HRF offers a more scalable alternative that recovers all the amplitudes at once instead of running QAE repetitively. This makes HRF particularly well suited for near-term quantum applications. A detailed comparison is provided in [table II](#).

Feature	QAE	HRF
Objective	Estimate single amplitude of general complex quantum states	Reconstruct full state vector of real-valued quantum states
Circuit Depth	Deep (uses Grover-like subroutines)	Shallow (single-layer Hadamards)
Measurements	Controlled unitaries with ancilla	σ_z, σ_x only
Qubit Overhead	$N_q + 1$ or more (ancilla + control)	N_q
Sample Complexity	Optimal $\mathcal{O}(1/\epsilon)$	Trade more samples for shallow circuits
NISQ Suitability	Low; Error-prone	High; Error-robust

TABLE II: Comparison between Quantum Amplitude Estimation (QAE) and Hadamard Random Forest (HRF).

Quantum State Overlap Estimation

Here, we show a concrete example of how HRF can simplify the task of estimating the overlap $S = |\langle \psi | \phi \rangle|^2$ between two unknown quantum states $|\psi\rangle$ and $|\phi\rangle$. Such a task has applications in quantum machine learning [46, 47] and cross-platform verification [48]. A widely adopted approach to this problem is the SWAP test [45], which involves applying a controlled-SWAP operation and measuring an ancillary qubit (see fig. 7). However, the SWAP test requires direct preparation and entanglement between the two states, making its implementation resource-intensive on near-term devices.

The HRF offers an alternative method for estimating state overlap. Instead of requiring entanglement between $|\psi\rangle$ and $|\phi\rangle$, HRF reconstructs each state independently and computes their overlap classically via post-processing of reconstructed amplitudes. This approach significantly reduces the circuit size by half. It also eliminates the need for controlled-SWAP operations, making it more scalable and implementable for near-term quantum hardware. In larger circuits, like the SWAP test, noise accumulates. Since HRF uses smaller circuits, it is more resilient to noise and can integrate well-established error mitigation methods such as SPAM error cancellation, as demonstrated in this work. The lower circuit complexity also opens up the possibility of further noise reduction techniques.

Regarding sample complexity and scalability, suppose there are R states. The swap test requires circuits involving all R^2 pairs of states, whereas HRF only needs to characterize each of the R states individually, leading to a quadratic speedup in terms of the number of states. We note, however, that HRF shifts the expensive cross-state quantum operations into classical post-processing, with a trade-off of potentially more measurement shots. Thus, HRF is more

advantageous for near-term devices where minimizing quantum circuit depth is crucial. Beyond state overlap estimation, the advantage brought by HRF can also generalize to other tasks involving multi-state property estimation, such as entanglement estimation [49, 50].

In this study, we apply the SWAP test to estimate overlap that resembles a numerical integration over the path ℓ_{N_q} . More specifically, the index state that encodes the 4-qubit path ℓ_4 is shown below

$$|\psi_{\ell_4}\rangle = \frac{1}{2\sqrt{2}}(|0001\rangle + |0010\rangle + |0100\rangle + |0111\rangle + |1000\rangle + |1011\rangle + |1101\rangle + |1110\rangle). \quad (\text{A1})$$

This happens to be a stabilizer state with $M_2(|\psi_{\ell_4}\rangle) = 0$ but more generally $|\psi_{\ell_6}\rangle$ is not a stabilizer state.

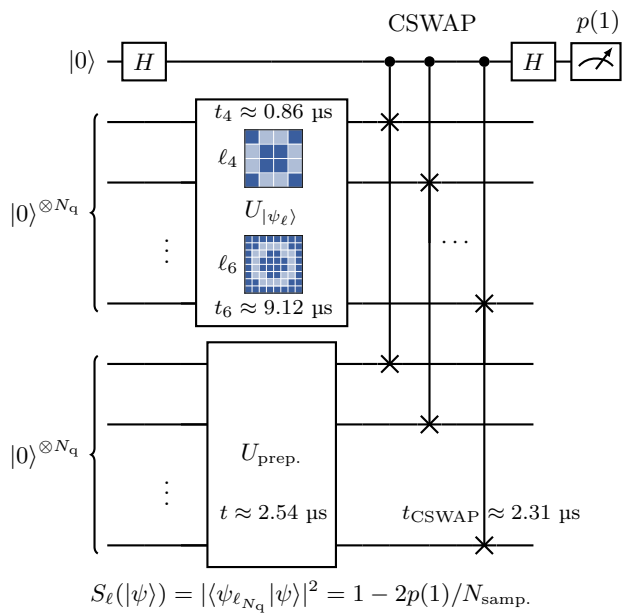


FIG. 7: SWAP test for estimating overlap $S_\ell(|\psi\rangle)$ with transpiled execution time on `ibm_fez` for each block.